PHYSICAL REVIEW C **102**, 054307 (2020)

In-gas-cell laser resonance ionization spectroscopy of ^{196,197,198}Ir

M. Mukai,[1,2,3,*] Y. Hirayama,[3] Y. X. Watanabe,[3] S. Schiffmann,[4,5] J. Ekman,[6] M. Godefroid,[5] P. Schury,[3]
Y. Kakiguchi,[3] M. Oyaizu,[3] M. Wada,[3] S. C. Jeong,[7] J. Y. Moon,[7] J. H. Park,[7] H. Ishiyama,[1] S. Kimura,[1] H. Ueno,[1]
M. Ahmed,[2] A. Ozawa,[2] H. Watanabe,[8] S. Kanaya,[9] and H. Miyatake[3]
[1]*Nishina Center for Accelerator-Based Science, RIKEN, Wako, Saitama 351-0198, Japan*
[2]*Graduate School of Pure and Applied Sciences, University of Tsukuba, Tsukuba, Ibaraki 305-0006, Japan*
[3]*Wako Nuclear Science Center (WNSC), Institute of Particle and Nuclear Studies (IPNS), High Energy Accelerator Research Organization (KEK), Wako, Saitama 351-0198, Japan*
[4]*Division of Mathematical Physics, Department of Physics, Lund University, SE-22100 Lund, Sweden*
[5]*Spectroscopy, Quantum Chemistry and Atmospheric Remote Sensing (SQUARES), CP160/09, Université libre de Bruxelles, B-1050 Brussels, Belgium*
[6]*Materials Science and Applied Mathematics, Malmö University, S-20506 Malmö, Sweden*
[7]*Rare Isotope Science Project, Institute for Basic Science (IBS), Daejeon 305-811, Republic of Korea*
[8]*IRCNPC, School of Physics and Nuclear Energy Engineering, Beihang University, Beijing 100191, China*
[9]*Department of Physics, Osaka University, Toyonaka, Osaka 563-0043, Japan*

(Received 10 September 2019; revised 6 August 2020; accepted 24 September 2020; published 4 November 2020)

Hyperfine structure (HFS) measurements of neutron-rich iridium isotopes ^{196,197,198}Ir ($Z = 77$, $N = 119$–121) were performed via in-gas-cell laser resonance ionization spectroscopy at the KEK Isotope Separation System. Magnetic dipole moments μ and isotope shifts were determined from the HFS spectra. The variation of mean-square charge radii and quadrupole deformation parameters of these isotopes were evaluated from the isotope shifts. The μ value of ^{197}Ir agreed with a theoretical value based on the strong coupling model, and the Ir nucleus was interpreted as prolately deformed by the theoretical calculations. The μ values of ^{196,198}Ir were also compared with semiempirical values calculated based on the strong coupling model. From the comparison, we can suggest the possible spin values of $I^{\pi} = 1, 2^{-}$ for ^{196}Ir and $I^{\pi} = 1^{-}$ for ^{198}Ir.

DOI: 10.1103/PhysRevC.102.054307

I. INTRODUCTION

The β-decay half-lives of waiting-point nuclei with neutron magic number $N = 126$ are needed to examine the time-scale of rapid neutron capture process (r process) and to estimate astrophysical environments from the simulated element abundances around the third peak originating from the r process [1,2]. However, the waiting-point nuclei of the third peak, defined by an atomic number $Z \approx 70$ and $N = 126$, are too far from the β-stability line, making difficult to access them experimentally. Therefore, reliable theoretical models are required for an accurate prediction of β-decay half-lives of the waiting-point nuclei. To establish those models, it is important to understand the competition between Gamow-Teller and first-forbidden transitions of β decay, which are sensitive to the structure of the relevant nuclei.

Laser spectroscopy can be used to investigate nuclear structure by providing information on the nuclear spin and nuclear electromagnetic moments, which are sensitive to the nuclear wave functions, and the variations of nuclear mean-square charge radii and quadrupole deformation parameters. Nuclear spin and electromagnetic moments can be directly determined from hyperfine structure (HFS) spectroscopy, and the variation of nuclear mean-square charge radii are calculated from isotopic energy shifts.

A systematic measurement of electromagnetic moments for the neutron-deficient and stable isotopes of $^{182-193}$Ir was performed via laser spectroscopy [3]. The neutron-deficient iridium isotopes were decay daughters of mercury isotopes that were produced by a spallation reaction between a proton beam and a lead target. The sudden change in the quadrupole deformation parameter between heavier ($187 \leqslant A \leqslant 193$) and lighter ($A \leqslant 186$) groups was similar to that observed in previous works on neutron-deficient isotopes of mercury, gold, and platinum [3]. This change was interpreted as a transition of the γ-soft shape to the axial symmetric prolate shape associated with the transition of the proton orbit from $3/2^{+}[402]$ of $A \geqslant 187$ nuclei to $1/2^{-}[541]$ of $A \leqslant 186$ nuclei. The experimental nuclear quadrupole deformation parameters of mercury, gold, platinum, and iridium approach the value of the spherical shape with increasing neutron number [3–6]. However, for iridium isotopes, the finite-range droplet model (FRDM) [7] predicted the shape transition from prolate ($A \leqslant 196$) to oblate ($A \geqslant 197$) at $A = 197$. We have investigated the evolution of nuclear deformation of iridium isotopes, $^{196-198}$Ir ($Z = 77$, $N = 119, 120, 121$), with in-gas-cell laser ionization spectroscopy as the first step of a systematic study of

---

[*] momo.mukai@riken.jp

nuclear structures for nuclei with $N \approx 126$ at the KEK Isotope Separation System (KISS) [8–10].

β decays were observed previously for these nuclei and the half-lives are known [11–13]. The nuclear spin-parity I^π appeared to be $I^\pi = (0^-)$ for ^{196}Ir from the log-ft values of ^{196}Ir β decays [14], and $I^\pi = 3/2^+$ for ^{197}Ir from the angular distributions of cross sections and analyzing powers [15]. In the present work, we report the magnetic dipole moments, mean-square charge radii, and nuclear quadrupole deformation parameters for these nuclei, as determined from HFS measurements.

II. LASER SPECTROSCOPY FOR HYPERFINE STRUCTURE MEASUREMENTS

The interaction between an electromagnetic field induced by orbital electrons and nuclear electromagnetic moments creates a hyperfine structure in the atomic state [16]. A consequence of the interaction is a new angular momentum $\boldsymbol{F}$ resulting from the coupling of the total angular momentum of the orbital electrons $\boldsymbol{J}$ and the nuclear spin $\boldsymbol{I}$ as $\boldsymbol{F} = \boldsymbol{I} + \boldsymbol{J}$. The quantum number of $\boldsymbol{F}$ can be any integer in the range $|J - I| \leqslant F \leqslant J + I$. The number of hyperfine levels governed by F is $2I + 1$ for $I \leqslant J$ and $2J + 1$ for $I > J$.

Energy splitting (ΔE) between hyperfine levels is expressed as a sum of energy shifts caused by the magnetic dipole interaction and the electric quadrupole interaction as follows:

$$\Delta E = \frac{A}{2} \times K + \frac{B}{2} \times \frac{3K(K+1) - 2I(I+1)2J(J+1)}{2I(2I-1)2J(2J-1)},$$
$$K = F(F+1) - I(I+1) - J(J+1). \tag{1}$$

A and B are the hyperfine coupling constants of the magnetic dipole and electric quadrupole interactions, respectively. The hyperfine coupling constants are given by

$$A = \frac{\mu H_J(0)}{IJ}, \tag{2}$$

$$B = eQ\phi_J(0). \tag{3}$$

$H_J(0)$ and $\phi_J(0)$ are the time-averaged magnetic field and the time-averaged electric field gradient generated by the orbital electrons at the nucleus, respectively.

The hyperfine interaction between a nucleus and the orbital electrons results in atomic energy shifts in the ground and excited states, indicated by $\Delta E_{\mathrm{g.s.}}$ and ΔE_{ex}, respectively. Thus, each transition frequency ν_i between corresponding hyperfine levels of the ground and excited states is given by

$$\nu_i = \frac{\Delta E_{\mathrm{ex},i} - \Delta E_{\mathrm{g.s.},i}}{h} + \nu_0, \tag{4}$$

where ν_0 is the transition frequency between the fine structure levels of the ground and excited states, and h is Planck's constant. The transition frequency ν_i is obtained from laser ionization spectroscopy by measuring the ion yield or the number of radioactive decays as a function of the excitation laser wavelength.

In the hyperfine spectrum analysis, we assumed that $H_J(0)$ and $\phi_J(0)$ are specific for each atomic state and are common in an isotope chain. Therefore, the nuclear magnetic dipole moment μ and electric quadrupole moment Q can be evaluated from the measured A and B, respectively, by using the known values of reference isotope (normally stable isotopes) A_{ref}, B_{ref}, I_{ref}, μ_{ref}, and Q_{ref} as follows:

$$\mu = \frac{I}{I_{\mathrm{ref}}} \frac{A}{A_{\mathrm{ref}}} \mu_{\mathrm{ref}}, \tag{5}$$

$$Q = \frac{B}{B_{\mathrm{ref}}} Q_{\mathrm{ref}}. \tag{6}$$

Here, the stable nucleus ^{191}Ir ($I^\pi = 3/2^+$) was used as the reference nucleus. If there is no experimental information about the A_{ref}, B_{ref} values, for example, in the cases of the reference isotopes with $I = 0$ or $1/2$, we could not apply Eqs. (5) and /or (6) to evaluate the μ and/or Q values from the measured A and/or B values. However, in such cases, we can compute $H_J(0)$ and $\phi_J(0)$ [17,18] precisely and derive μ and Q values from the measured A and B values, respectively.

Finite nuclear mass and size cause ν_0 shifts between the isotopes. Hence, variations in the nuclear mean-square charge radius and the nuclear quadrupole deformation parameter can be determined from the shift between two isotopes with mass numbers A and A', $\delta\nu_{\mathrm{IS}}^{AA'} = \nu_0^{A'} - \nu_0^{A}$ $(A' > A)$. Details of the isotope shift are discussed below in Sec. V A.

III. EXPERIMENT

A. KEK isotope separation system

The experiments were performed using KISS [8–10], an argon-gas-cell-based laser ion source combined with an online isotope separator, installed at the RIBF facility of the RIKEN Nishina center. Unstable iridium isotopes were produced as target-like fragments (TLFs) via multinucleon transfer (MNT) reactions of ^{136}Xe + ^{198}Pt [19]. The ^{136}Xe primary beam (10.75 MeV/nucleon, 50 particle-nA), accelerated by the RIKEN Ring Cyclotron, impinged on an energy degrader that consisted of three 3 μm-thick titanium foils (9 μm in total) that optimized the reaction energy by reducing the beam energy to 9.4 MeV/nucleon. Then, the beam impinged on a ^{198}Pt target (12.5 mg/cm^2 in thickness).

The TLFs were accumulated, thermalized, and neutralized in the argon gas cell at a 74 kPa pressure optimized for the TLF stopping efficiency. The neutralized TLFs exited the gas cell via laminar argon gas flow. The iridium atoms were element-selectively reionized just before the gas cell exit via two-color, two-step laser resonance ionization. The singly charged iridium ions were accelerated with an energy of 20 keV, and their mass-to-charge ratios were selected with a dipole magnet. Finally, the purified radioactive beam was transported to a detector station that included a tape transport device for avoiding radioactivity in the decay chain of the separated nuclide under pulsed beam operation of KISS. The radioactive isotope was implanted in an aluminized mylar tape of the tape transport device, which was surrounded by β-ray detectors [20,21].

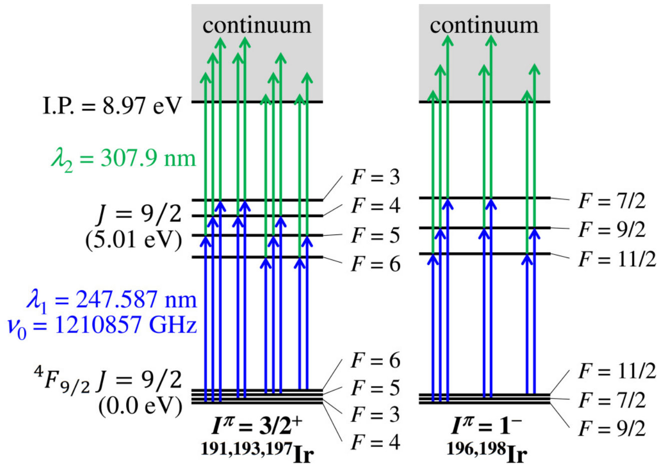

FIG. 1. Ionization schemes and hyperfine structures of iridium isotopes. The total angular momentum of the atomic state is $J = 9/2$ for both ground and excited states. For ^{191,193}Ir (stable) and ^{197}Ir with known $I^\pi = 3/2^+$, the hyperfine splitting of $F = 3, 4, 5, 6$ appears in both ground and excited states, with ten transitions (left). For ^{196,198}Ir with the assumption of $I^\pi = 1^-$, the hyperfine splitting of $F = 7/2, 9/2, 11/2$ appears in both ground and excited states, with seven transitions (right).

B. Laser ionization schemes

An excitation laser with wavelength λ_1 and an ionization laser with wavelength λ_2 were used for the ionization spectroscopy. Figure 1 depicts the ionization schemes and the hyperfine structures of the iridium isotopes. The excitation transition was $5d^76s^2\ ^4F_{9/2} \rightarrow 9/2^\circ$ ($\lambda_1 = 247.587$ nm, 40389.83 cm^{-1}, 5.01 eV) [22]. The Einstein coefficient A_{ki} of the transition is 2.04×10^7 s^{-1} [23]. The hyperfine coupling constants $A^{191}_{\rm gs} = +57.52128(3)$ MHz and $B^{191}_{\rm g.s.} = +471.2045(3)$ MHz were known for the stable isotope ^{191}Ir [24]. $A^{191}_{\rm ex}$ and $B^{191}_{\rm ex}$ were determined here to be $A^{191}_{\rm ex} = -529^{+42}_{-37}$ MHz and $B^{191}_{\rm ex} = +1893^{+1016}_{-931}$ MHz. Even though the measured $B^{191}_{\rm ex}$ value had a large uncertainty because of unresolved HFS spectra acquired by in-gas-cell laser ionization spectroscopy, it did not affect the determination of the unknown $A_{\rm g.s.,ex}$ values of the unstable isotopes $^{196-198}$Ir.

The dye laser (Radiant Dyes, NarrowScan) was pumped by an excimer laser (XeCl, 307.9 nm, 4.03 eV, Lambda Physik, LPX240i) to generate a fundamental wavelength $2\lambda_1 \approx 500$ nm by using a dye solution of Coumarin 500. The fundamental wavelength was frequency doubled with a barium borate oxide (BBO) crystal placed in a second-harmonic generator (SHG), and finally the wavelength of $\lambda_1 \approx 247.587$ nm at a power of 100 μJ/pulse was obtained. For ionization to the continuum, another excimer laser was used at $\lambda_2 = 307.9$ nm with a power of 12 mJ/pulse. The pulse width of the two lasers was about 15 ns full width at half-maximum (FWHM), while the FWHM line width of the excitation laser was 3.4 GHz. The 100 Hz repetition rate was high enough for the temporal overlap between the laser pulses and the atoms given the atom velocity in the laminar gas flow [8].

During the experiment, laser timing, position, power, and wavelength were monitored and optimized as follows. Timing between the fundamental dye laser light ($2\lambda_1$) and the excimer laser (λ_2) was monitored with photodiodes (Electro-Optics Technology Inc., ET3020) and optimized with external trigger signals of two excimer lasers to maximize the ion yield. Moreover, the timing was adjusted to avoid the distortion of HFS spectra stemmed from the intense ionization laser field [25]. We confirmed there was no distortion in the present measurements. The spatial overlap of the two laser beams in the gas cell was also adjusted to maximize the ion yield. A small part of the fundamental dye laser was monitored with a power meter (J-25MB-LE, Coherent). The powers of both lasers were higher than that needed for saturation of the transitions, and fluctuations were less than 10%. The wavelength $2\lambda_1$ was monitored by sampling 1% fraction of the laser beam with a wave meter WS6 (HighFinesse).

C. Experimental procedures

1. *Confirmation of* ^{196,197,198}Ir *extractions*

The extractions of ^{196,197,198}Ir were confirmed from half-lives ($T_{1/2}$) measured by β-ray detectors [20,21]. The radioactive nuclei purified by KISS were implanted on the tape during a beam-on period $T_{\rm on} = 1.5 \times T_{1/2}$. The implantation of the radioactive nuclei was suspended during a beam-off period $T_{\rm off} = 4 \times T_{1/2}$ to measure the half-lives of the iridium isotopes implanted on the tape. Just before every $T_{\rm on}$ period, the tape was moved 30 cm during $T_{\rm move} = 1$ s to remove activities from daughter nuclei.

Growth- and decay-time spectra are shown in Fig. 2. To identify the isotopes from the half-life fits, the isomer components of each isotope had to be considered. Isomers with a half-life longer than several hundred ms can be produced by the MNT reactions and extracted from KISS, as reported in Ref. [26]. The isomeric states of ^{196,197}Ir were reported previously [11,12], while those of ^{198}Ir were not reported. The level energy, half-life, and the β-decay branching ratio of the isomers were, respectively, $E = 410(110)$ keV, $T_{1/2} = 1.40(2)$ h, and $\approx$100% for the $^{196\rm m}$Ir isomer [11], and $E = 115(5)$ keV, $T_{1/2} = 8.9(3)$ min, and 99.75(10)% for the $^{197\rm m}$Ir isomer [12].

The half-life of $^{196\rm m}$Ir was much longer than that of the $^{196\rm g}$Ir ground state $T_{1/2} = 52(1)$ s [11], and, therefore, the component of $^{196\rm m}$Ir in the spectrum was negligible. Because the daughter nucleus ^{196}Pt is stable, the half-life and implantation intensity of the ground state, and the background event rate were treated as free parameters to fit the growth- and decay-time spectrum of ^{196}Ir. The same method was applied to the spectrum of ^{198}Ir, which has a stable ^{198}Pt daughter nucleus. The half-life of $^{197\rm m}$Ir was similar with $T_{1/2} = 5.8(5)$ min [12] of $^{197\rm g}$Ir, and, therefore, the component of $^{197\rm m}$Ir in the spectrum was taken into account. In the fits, the half-lives of $^{197\rm m}$Ir and $^{197\rm g}$Ir were constrained to reported values of $T_{1/2}$ within the reported uncertainties $\delta T_{1/2}$ [12]. The yield ratio R of $^{197\rm g}$Ir to $^{197\rm g+m}$Ir and the background event rate were treated as the free parameters in the fits. The half-life of the daughter nuclei ($^{197\rm g}$Pt) was fixed to the literature value $T_{1/2} = 19.8915(19)$ h [12].

The results of the half-life analyses are summarized in Table I. The spectra of ^{196,197,198}Ir in Fig. 2 were well fit (solid lines) with reduced χ^2 values of 1.1, 0.8, and 0.9, respectively.

TABLE I. Analyses results for the growth- and decay-time spectra of ^{196,197,198}Ir in Fig. 2. The extraction yields were corrected by the detection efficiency of the β-ray detectors. The ^{197}Ir analysis was performed using constrained half-lives $T_{1/2} \pm \delta T_{1/2}$ for $^{197\text{g,m}}$Ir to determine the yield ratio R of $^{197\text{g}}$Ir to $^{197\text{g+m}}$Ir. The extraction yield of ^{197}Ir in the table was the sum of those of $^{197\text{g}}$Ir and $^{197\text{m}}$Ir. The yield ratio R was $0.9^{+0.1}_{-0.4}$.

Nuclide	Reduced χ^2	Measured half-life	Reported half-life	Extraction yield (pps)
^{196}Ir	1.1	49(5) s	52(1) s [11]	10(1)
^{197}Ir	0.8	–	5.8(5) min [12]	9(1)
^{198}Ir	0.9	8.9(4) s	8(1) s [13]	4.9(3)

The determined half-lives of $T_{1/2} = 49(5)$ s for ^{196}Ir and $T_{1/2} = 8.9(4)$ s for ^{198}Ir were well consistent with literature values of $T_{1/2} = 52(1)$ s for ^{196}Ir [11] and $T_{1/2} = 8(1)$ s for ^{198}Ir [13], respectively. The yield ratio R was $0.9^{+0.1}_{-0.4}$ for ^{197}Ir. The extraction yields shown in Table I were evaluated from fitted values by accounting for the detection efficiency of the β-ray detectors. Yields $\geqslant 5$ pps were high enough for HFS measurements on these isotopes. Finally, the extraction of $^{196\text{g},197\text{g},198\text{g}}$Ir from the KISS gas cell was confirmed.

2. Acquisition of HFS spectra

To analyze the HFS spectra of ^{196,197,198}Ir accurately, the spectrum of the stable isotope ^{191}Ir was acquired to determine the hyperfine coupling constants (A_{ex} and B_{ex}) and the response function of the in-gas-cell laser ionization spectroscopy in the present experimental condition. Neutral atoms of the stable isotope were obtained by resistive heating of an iridium filament installed in the KISS gas cell. Figure 3 plots the HFS spectra for ^{191,196,197,198}Ir obtained by measuring the extracted ion yields as a function of excitation laser wavelength. For ^{191}Ir, the laser-ionized atoms were detected with a multichannel plate that was upstream from the KISS detector station. Extraction yields of the unstable isotopes were evaluated by analyzing the growth time spectra of β rays. Fluctuations of the primary beam intensity during T_{on} were considered in the error analysis of the extraction yield. The yield at each excitation laser wavelength was corrected for the primary beam dose. Details in HFS analyses are discussed in Secs. IV A and IV B.

IV. ANALYSIS

A. Response functions and hyperfine coupling constants

The HFS line-shape for each transition is expressed by the Voigt function, which consists of Gaussians and Lorentzians [27]. The Voigt profile is common for all the transitions. In in-gas-cell laser ionization spectroscopy, two Gaussian components stem from the line width of the excitation laser (3.4 GHz) and Doppler broadening at the gas temperature of 300 K (1.1 GHz) [26], and three Lorentzian components stem from the natural line width (3.3 MHz) of an atomic excited state, pressure broadening, and laser-power broadening [28]. The laser-power and pressure broadenings strongly depend on the experimental condition such as the gas cell pressure and laser powers, and should be measured to determine the response function. Their sum $\Gamma_{\text{L},74\,\text{kPa}}$ was determined from the HFS spectrum of stable ^{191}Ir.

The absorption line width ($\approx$10 GHz) of the iridium atoms was much broader than the energy shifts ($\leqslant 5.5$ GHz) caused by the hyperfine interactions. Therefore, the peak height was proportional to the relative transition probability [29], calculated from the statistical weight $(2F+1)$ of each hyperfine level. The peak height is given by

$$\frac{2F_{\text{g.s.},i}+1}{\Sigma_j(2F_{\text{g.s.},j}+1)}\,\frac{2F_{\text{ex},k}+1}{\Sigma_l(2F_{\text{ex},l}+1)}\times f_{\text{amp}}, \tag{7}$$

for the transition between the ith hyperfine level in the ground state and the kth hyperfine level in the excited state. $F_{\text{g.s.},j}$ is the total angular momentum of the jth hyperfine level in the ground state. $F_{\text{ex},l}$ is the total angular momentum of the lth hyperfine level in the excited state, which can be populated from $F_{\text{g.s.},i}$ by the excitation laser. f_{amp} is a common coefficient for all transitions to fit the HFS spectra, and is used as one of the free parameters.

The background level and the frequency $\nu^{A}_{\text{obs.}}$ (= center-of-gravity frequency + arbitrary offset) were also treated as free parameters to fit the HFS spectra. The arbitrary offset was common for all the isotopes. The isotope shift was then determined from $\delta\nu^{191,A'}_{\text{IS}} = \nu^{A'}_{\text{obs.}} - \nu^{191}_{\text{obs.}}$.

The fitting analysis was performed with ROOT [30] and the MINUIT library [31] for statistical error analysis. The MINOS option was used to calculate asymmetric parameter errors. The Voigt function was provided in the mathematical library of ROOT. Errors of the fitting parameters shown in below were increased by considering the square root of the resultant reduced χ^2 value.

Parameters associated with the HFS spectra are summarized in Table II. A^{191}_{ex}, B^{191}_{ex}, and $\Gamma_{\text{L},74\,\text{kPa}}$ were derived from fitting the HFS spectrum of ^{191}Ir at an argon gas pressure of 74 kPa, as shown in Fig. 3(a). B^{191}_{ex} had a large uncertainty because of pressure and power broadenings. The A_{ex} and B_{ex} values for the other isotopes were calculated according to Eqs. (5) and (6) by using known $\mu_{\text{ref}} = +0.1507(6)\ \mu_{\text{N}}$ [24] and $Q_{\text{ref}} = +0.816(9)$ b [32] for ^{191}Ir and analyzed values of μ and Q for ^{196,197,198}Ir. The fitting procedure for the HFS spectra of ^{196,198}Ir was performed by assuming spin values $I = 0, 1, 2$, or 3, and the most probable spin value was indicated from the minimum reduced χ^2.

TABLE II. Summary of HFS parameters for iridium isotopes. The μ, Q, $A_{\mathrm{g.s.}}$, and $B_{\mathrm{g.s.}}$ values of the stable isotope ^{191}Ir were precisely measured in Refs. [24,32]. The $A_{\mathrm{g.s.}}$, $B_{\mathrm{g.s.}}$, A_{ex}, and B_{ex} values of $^{196\text{–}198}$Ir are determined by using the other parameters indicated in the parenthesis. The Lorentz width $\Gamma_{\mathrm{L,74\,kPa}}$ consisted of power and 74 kPa argon gas pressure broadenings. A^{191}_{ex}, B^{191}_{ex}, and $\Gamma_{\mathrm{L,74\,kPa}}$ were determined from the fitting of HFS spectrum of ^{191}Ir. These three values are commonly used to determine the $\delta\nu^{191,A'}_{\mathrm{IS}}$, μ, Q, and I values of $^{196\text{–}198}$Ir.

	^{191}Ir	^{196}Ir	^{197}Ir	^{198}Ir
I^{π}	$3/2^{+}$	(0^{-})	$3/2^{+}$	unknown
μ (μ_{N})	+0.1507(6) [24]		$\mu^{A'}$	
Q (b)	+0.816(9) [32]		$Q^{A'}$	
$A_{\mathrm{g.s.}}$ (MHz)	+57.52128(3) [24]		$A^{A'}_{\mathrm{g.s.}}(A^{191}_{\mathrm{g.s.}}, I^{191}, \mu^{191}, I^{A'}, \mu^{A'})$	
$B_{\mathrm{g.s.}}$ (MHz)	+471.2045(3) [24]		$B^{A'}_{\mathrm{g.s.}}(B^{191}_{\mathrm{g.s.}}, Q^{191}, Q^{A'})$	
A_{ex} (MHz)	$A^{191}_{\mathrm{ex}} = -529^{+42}_{-37}$		$A^{A'}_{\mathrm{ex}}(A^{191}_{\mathrm{ex}}, I^{191}, \mu^{191}, I^{A'}, \mu^{A'})$	
B_{ex} (MHz)	$B^{191}_{\mathrm{ex}} = +1893^{+1016}_{-931}$		$B^{A'}_{\mathrm{ex}}(B^{191}_{\mathrm{ex}}, Q^{191}, Q^{A'})$	
$\delta\nu^{191,A'}_{\mathrm{IS}}$ (GHz)	0		$\delta\nu^{191,A'}_{\mathrm{IS}}$	
$\Gamma_{\mathrm{L,74\,kPa}}$ (GHz)		$9.2^{+1.1}_{-1.0}$		

B. μ and $\delta\nu_{\mathrm{IS}}$ values for ^{196,197,198}Ir

The HFS spectra of ^{196,197,198}Ir were analyzed individually with fitting parameters μ, Q, $\nu^{A'}_{\mathrm{obs.}}$, f_{amp}, and the background level. A^{191}_{ex}, B^{191}_{ex}, and $\Gamma_{\mathrm{L,74\,kPa}}$ were considered as constrained parameters within a margin of two sigma ($\pm 2\sigma$). In HFS analyses with $I = 0$, $\nu^{A'}_{\mathrm{obs.}}$, f_{amp}, background level, and $\Gamma_{\mathrm{L,74\,kPa}}$ were used as free parameters.

In the cases of ^{196,198}Ir, the spin values were unknown. Therefore, the statistical analyses were performed by assuming spin values $I = 0, 1, 2$, or 3. The HFS spectra of ^{196,198}Ir with the best fitted curves are shown in Figs. 3(b) and 3(d), respectively. The results are summarized in Table III. When $I = 0$ was assumed, the widths of the spectra were broader than the $\Gamma_{\mathrm{L,74\,kPa}}$ value, and the minimum reduced χ^2 values became as large as 3.0 and 2.5 for ^{196}Ir and ^{198}Ir, respectively. Therefore, the spin value of both isotopes should be $I \geqslant 1$. The Q values of ^{196}Ir and ^{198}Ir were not determined accurately by using the B^{191}_{ex} value because of its large uncertainty.

For $^{197\mathrm{g}}$Ir, the spin value $I^{\pi} = 3/2^{+}$ was reported in Ref. [12]. Therefore, ten HFS transitions were considered in the analysis. The fraction of isomer $^{197\mathrm{m}}$Ir in the ^{197}Ir beam was $0.1^{+0.4}_{-0.1}$, as determined from the half-life analysis in Sec. III C 1. The expected ten hyperfine transitions of $^{197\mathrm{m}}$Ir were widely spread over the range 400 GHz because of the large $I^{\pi} = 11/2^{-}$ and $\mu \approx 6$ μ_{N} expected from the systematic trend of the measured μ values for the $I^{\pi} = 11/2^{-}$ state. No HFS peaks for $^{197\mathrm{m}}$Ir were observed, indicating no $^{197\mathrm{m}}$Ir-contamination. Hence the $^{197\mathrm{m}}$Ir HFS component was negligible. The μ and $\delta\nu^{191,197}_{\mathrm{IS}}$ values of $^{197\mathrm{g}}$Ir were $\mu = +0.27^{+0.10}_{-0.03}$ μ_{N}, $\delta\nu^{191,197}_{\mathrm{IS}} = -10.3(7)$ GHz with the minimum reduced $\chi^2 = 1.8$. The Q value of $^{197\mathrm{g}}$Ir was not determined accurately by using the B^{191}_{ex} value because of its large uncertainty.

V. DISCUSSION

A. Charge radii and deformation parameters

The variations of the nuclear mean-square charge radius $\delta\langle r^2_{\mathrm{c}}\rangle$ and the nuclear quadrupole deformation parameter β_2 were calculated from the measured isotope shifts [3,33]. The isotope shift between two isotopes with mass numbers A and A' ($A' > A$) consists of a mass shift $\delta\nu^{AA'}_{\mathrm{MS}}$ and a field shift $\delta\nu^{AA'}_{\mathrm{FS}}$, induced by the change in reduced mass of a nucleus-electron system and the change in nuclear size, respectively.

TABLE III. Magnetic dipole moments μ and isotope shifts $\delta\nu^{191,A'}_{\mathrm{IS}}$ of ^{196,198}Ir ground states assuming nuclear spin I.

Nuclear	μ, $\delta\nu^{191,A'}_{\mathrm{IS}}$,	Values	
spin I	reduced χ^2	$A' = 196$	$A' = 198$
0	$\delta\nu_{\mathrm{IS}}$ (GHz)	$-5.7^{+1.2}_{-1.2}$	$-8.7^{+0.6}_{-0.6}$
	Reduced χ^2	3.0	2.5
1	μ (μ_{N})	$+0.31^{+0.04}_{-0.20}$	$+0.13^{+0.10}_{-0.02}$
	$\delta\nu_{\mathrm{IS}}$ (GHz)	$-7.3^{+0.6}_{-1.4}$	$-9.8^{+0.5}_{-0.3}$
	Reduced χ^2	1.4	1.1
2	μ (μ_{N})	$+0.34^{+0.05}_{-0.14}$	$+0.24^{+0.02}_{-0.09}$
	$\delta\nu_{\mathrm{IS}}$ (GHz)	$-7.0^{+0.7}_{-0.7}$	$-9.4^{+0.3}_{-0.3}$
	Reduced χ^2	1.8	1.4
3	μ (μ_{N})	$+0.36^{+0.07}_{-0.17}$	$+0.26^{+0.02}_{-0.09}$
	$\delta\nu_{\mathrm{IS}}$ (GHz)	$-7.0^{+0.8}_{-1.2}$	$-9.3^{+0.3}_{-0.3}$
	Reduced χ^2	1.9	1.4

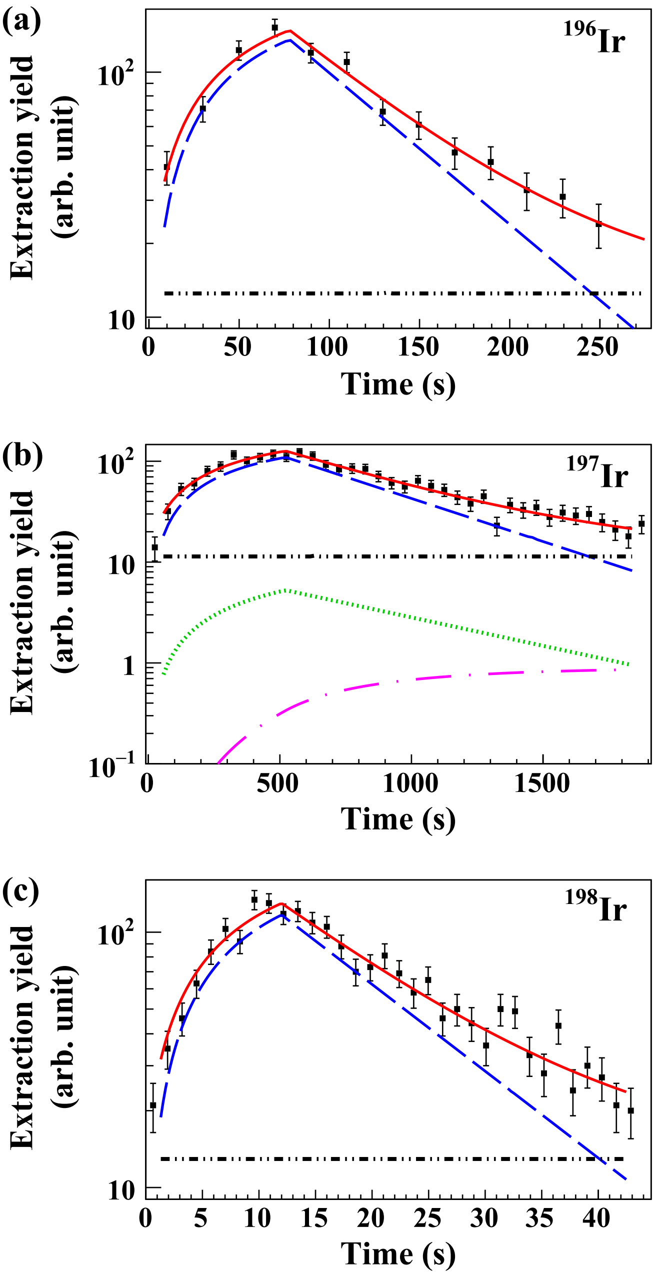

FIG. 2. Growth- and decay-time spectra of (a) ^{196}Ir, (b) ^{197}Ir, and (c) ^{198}Ir. The lines are the best fits to the experimental data. The two-dot chain (black), dashed (blue), and solid (red) lines indicate background events of the β-ray detectors, the growth and decay curves of each implanted nucleus (ground state), and the sum of all components, respectively. The dotted (green) and dashed-dotted (magenta) lines in the ^{197}Ir spectrum indicate the isomer ($^{197\mathrm{m}}$Ir) and the daughter ($^{197\mathrm{g}}$Pt) decay components, respectively.

Therefore, the isotope shift $\delta\nu_{\mathrm{IS}}^{AA'}$ is expressed as

$$\delta\nu_{\mathrm{IS}}^{AA'} = \delta\nu_{\mathrm{MS}}^{AA'} + \delta\nu_{\mathrm{FS}}^{AA'}. \quad (8)$$

The mass shift is expressed as the sum of the normal mass shift (NMS) and the specific mass shift (SMS) contributions,

$$\delta\nu_{\mathrm{MS}}^{AA'} = \delta\nu_{\mathrm{NMS}}^{AA'} + \delta\nu_{\mathrm{SMS}}^{AA'} = \left(\frac{1}{M_A} - \frac{1}{M_{A'}}\right)\delta K_{\mathrm{MS}}, \quad (9)$$

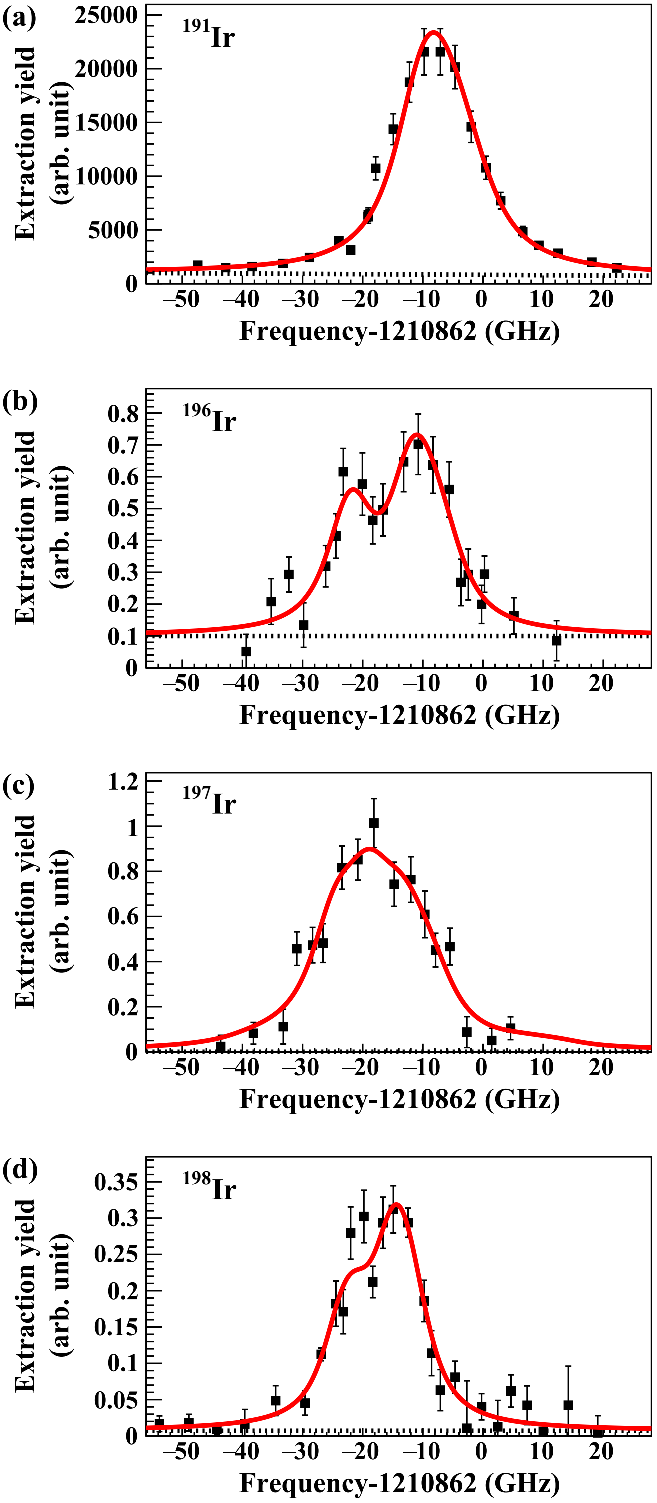

FIG. 3. HFS spectra of (a) ^{191}Ir, (b) ^{196}Ir, (c) ^{197}Ir, and (d) ^{198}Ir with the best fits (red solid lines). The black dotted lines indicate the fitted background level. The spectra were measured at an argon gas pressure of 74 kPa.

where M_A and $M_{A'}$ are the nuclear masses and δK_{MS} is the mass shift factor.

The field shift corresponds to the change in electron binding energy induced by the change in the nuclear charge distribution between two isotopes, due to the finite volume of the nucleus. The field shift is written as the products of line electronic factors ΔF_i ($i = 0, 2, 4, 6$) and difference in radial moments $\delta\langle r_c^N\rangle^{AA'}$ ($N = 2, 4, 6, 8$) [34] as given by

$$\delta\nu_{\mathrm{FS}}^{AA'} = \frac{\Delta F_0}{h}\delta\langle r_c^2\rangle^{AA'} + \frac{\Delta F_2}{h}\delta\langle r_c^4\rangle^{AA'} + \frac{\Delta F_4}{h}\delta\langle r_c^6\rangle^{AA'} + \frac{\Delta F_6}{h}\delta\langle r_c^8\rangle^{AA'}. \tag{10}$$

We can determine $\delta\langle r_c^2\rangle^{AA'}$ values from the measured isotope shift by using δK_{MS} and ΔF_i values which can be precisely determined through theoretical atomic calculations. The latter are briefly described in the following paragraphs. More details can be found in [35].

Large-scale atomic calculations were performed using the GRASP2018 collection of programs [36], based on the multiconfiguration Dirac-Hartree-Fock (MCDHF) theory [37] to compute the electronic field shift factors ΔF_0, ΔF_2, ΔF_4, and ΔF_6 [34] of the $5d^76s^2\ ^4F_{9/2} \rightarrow 9/2^\circ$ transition. Although the energy transition is well established at 40389.83 cm^{-1}, the upper level, corresponding to the sixth odd-parity $J = 9/2$ level, has not yet been identified with certainty [22,38,39].

Within the MCDHF framework, each atomic level is described by an atomic state function that is expanded over a linear combination of configuration state functions (CSFs), which are themselves built as antisymmetric sums of products of Dirac one-electron four-components spinors [40] with separate radial and angular parts. The CSF list is generated by electron substitutions from the reference configurations to a set of virtual orbitals, which are introduced to describe the electron correlation. The choice of the reference configurations is guided by previous works on Ir [22,41] and includes the $\{5d^76s^2,\ 5d^86s,\ 5d^9\}$ and $\{5d^76s6p,\ 5d^86p,\ 5d^66s^26p\}$ configurations for the even and odd parity, respectively. The radial part of the spectroscopic and correlation orbitals are obtained by solving the multiconfiguration Dirac-Hartree-Fock equations. The CSF expansion coefficients are estimated from the weighted sum of the targeted eigenvectors of the Dirac-Coulomb Hamiltonian matrix. This optimization process is repeated iteratively until self-consistency. Subsequent relativistic configuration interaction (RCI) calculations are performed to include higher order effects by adding the long-wavelength-approximation Breit interaction and QED operators to the Hamiltonian, or by enriching the CSFs basis set by allowing other kinds of electron substitutions.

The quality of our wave functions can be assessed by comparing the calculated energy spectrum to the observed one. In the case of neutral iridium, the energy spectrum is particularly difficult to calculate accurately because i) its ground configuration has an open d shell, which gives rise to a large number of CSFs, ii) the excitation energy of the first excited state (even, $J = 9/2$) is small and therefore a strong interaction with the ground state is expected, iii) strong mixing is observed among all odd-parity levels, iv) a "root-flipping" is observed for the sixth and seventh levels [35], as the computed level might not match the level involved in the measured transition, i.e., that its position in the theoretical Hamiltonian spectrum of the ordered roots of the (π, J) block symmetry does not correspond to its position in the energy-ordered experimental spectrum. The root-flipping between the targeted sixth lowest level and the seventh lowest level is particularly critical as their configuration compositions differ substantially. According to the Bauche and Champeau "sharing rule" [42], the relative weight of the leading configurations strongly influence the field shift parameter [43]. A detailed analysis based on the Landé g factors and the relative phases of the leading CSFs allowed us to unambiguously detect the root-flipping (for more details, see [35]).

Once we have obtained the mixing coefficients and orbital basis, we can evaluate the expectation value of any operator, such as the isotope shift parameters or hyperfine structure constants. The isotope field shift of the transition was computed according to the RIS4 [34] formalism, that goes beyond the approximation of a constant electron density inside the nuclear volume. The electron density of the state i is fitted to an even polynomial series as $\rho_i^e(\mathbf{r}) = \sum_{n=0}^{3} b_{i,2n} r^{2n}$, where the electronic parameters ΔF_{2n} are proportional to $b_{i,2n} - b_{j,2n}$, in which i and j are the two levels involved in the transition. We finally present the following electron computed isotope shift parameters:

$$\begin{aligned}
\Delta K_{247,\mathrm{MS}} &= 650(1000)\ \mathrm{GHz\ u}\ ,\\
\Delta F_{247,0} &= -48.1(3.0)\ \mathrm{GHz/fm^2}\ ,\\
\Delta F_{247,2} &= 0.0526\ \mathrm{GHz/fm^4}\ ,\\
\Delta F_{247,4} &= -0.000150\ \mathrm{GHz/fm^6}\ ,\\
\Delta F_{247,6} &= 0.000000267\ \mathrm{GHz/fm^8}\ ,
\end{aligned} \tag{11}$$

which confirm the negligible influence of the mass shift, e.g., $\nu_{247,\mathrm{MS}}^{191,193} = 0.04$ GHz compared to the measured IS $\nu_{247,\mathrm{IS}}^{191,193} = -3.0(2)$ GHz. No reliable uncertainties were found for the $\Delta F_{247,2}$, $\Delta F_{247,4}$, and $\Delta F_{247,6}$ parameters, as their values are highly dependent on each other and on $\Delta F_{247,0}$.

The $\delta\nu_{\mathrm{IS}}^{191,A'}$ and $\delta\nu_{\mathrm{FS}}^{191,A'}$ values of ^{193,196,197,198}Ir are listed in Table IV. The $\delta\nu_{\mathrm{IS}}^{191,A'}$ values of ^{196,198}Ir were taken from the best fit results with spin value $I = 1$.

We present here the details of the derivation of $\delta\langle r_c^2\rangle^{AA'}$ and β_2. The radial moments of the nuclear charge distribution $\langle r_c^N\rangle^A$ where computed assuming a three-parameter Fermi distribution

$$\rho^A(r,\theta) = \frac{\rho_0^A}{1 + \exp\left(\frac{r - c_{\mathrm{def}}^A[1 + \beta_2^A Y_{20}(\theta)]}{a}\right)}\ , \tag{12}$$

where ρ_0^A is a normalization constant, a is the skin diffuseness parameter related to the skin thickness $t = 4\ \ln(3)a$, and β_2^A is the axially symmetric quadrupole deformation. Assuming volume conservation (conservation of ρ_0^A), the nuclear size parameter c_{def}^A was iteratively determined for a given value of β_2^A as

$$c_{\mathrm{def}}^A = \left[\frac{\left(c_{\mathrm{sph}}^A\right)^3 + \pi^2 a^2\left(c_{\mathrm{sph}}^A - c_{\mathrm{def}}^A\right)}{1 + \frac{3}{4\pi}\left(\beta_2^A\right)^2 + \frac{1}{28\pi}\sqrt{\frac{5}{\pi}}\left(\beta_2^A\right)^3}\right]^{1/3}\ , \tag{13}$$

TABLE IV. The $\delta\langle r_c^2\rangle^{191,A'}$ and $|\beta_2|$ values of ^{193,196,197}Ir. The $\delta\nu_{\rm IS}^{191,A'}$ value of ^{196}Ir was taken from the best-fit result with spin value $I = 1$. The $|\beta_2|$ values were normalized to be $\beta_2 = +0.140$ at ^{191}Ir, which was calculated from the Q value.

A'	$\delta\nu_{\rm IS}^{191,A'}$ (GHz)	$\delta\nu_{\rm FS}^{191,A'}$ (GHz)	$\delta\langle r_c^2\rangle^{191,A'}$ (fm^2)	$\|\beta_2\|$
191	0	0	0	0.140(2)
193	$-3.0(2)$	$-3.0(2)$	$+0.065^{+0.007}_{-0.006}$	0.118(5)
196	$-7.3^{+0.6}_{-1.4}$	$-7.4^{+0.6}_{-1.4}$	$+0.16^{+0.03}_{-0.02}$	0.06(2)
197	$-10.3(7)$	$-10.4(7)$	$+0.23(2)$	0.07(2)

where $c_{\rm sph}^A$ was deduced from the mean-square radius as predicted from the droplet model [44]

$$\left(c_{\rm sph}^A\right)^2 = \frac{5}{3}\left\langle r_c^2\right\rangle_{\rm sph}^A. \tag{14}$$

Fixing the deformation of ^{191}Ir and thus $\langle r_c^N\rangle^{191}$, β_2^A (and consequently $\langle r_c^N\rangle^A$) was varied until the equality of Eq. (10) was obtained. The fixed β_2 value of ^{191}Ir was $+0.140(2)$ which was calculated from the previously measured spectroscopic quadrupole moment of $Q = +0.816(9)$ b [32] assuming $K = I = 3/2$. In the calculations, $t = 2.30$ fm was used for all isotopes and the electronic factors ΔF were computed using the RIS4 program [34] assuming for the nuclear charge distribution a Fermi distribution with $\langle r_c^2\rangle^{1/2} = 5.40$ fm and $t = 2.30$ fm.

The $\delta\langle r_c^2\rangle^{191,A'}$ and $|\beta_2|$ values were calculated to be

$$\delta\left\langle r_c^2\right\rangle^{191,193} = +0.065^{+0.007}_{-0.006}\ \text{fm}^2,\quad |\beta_2| = 0.118(5)$$

for ^{193}Ir,

$$\delta\left\langle r_c^2\right\rangle^{191,196} = +0.16^{+0.03}_{-0.02}\ \text{fm}^2,\quad |\beta_2| = 0.06(2)$$

for ^{196}Ir,

$$\delta\left\langle r_c^2\right\rangle^{191,197} = +0.23(2)\ \text{fm}^2,\quad |\beta_2| = 0.07(2)$$

for ^{197}Ir. Our $\delta\langle r_c^2\rangle^{191,193}$ value agreed with $\delta\langle r_c^2\rangle^{191,193} = +0.0691(8)$ fm^2 extracted from the measured isotopes shift value of 351.5 nm transition by Verney *et al.* [3]. However, the present $|\beta_2| = 0.118(5)$ is smaller than $\langle\beta_2^2\rangle^{1/2} = 0.144(1)$ extracted by Verney *et al.* The majority of this difference originates from the choice of the anchor value of β_2^{191} and the parameter values used in the droplet model. The values for ^{198}Ir were not obtained in our calculation using Berdichevsky's spherical charge radius calculated with the parameters shown in Eq. (3) in Ref. [44]. The calculation results are listed in Table IV and plotted in Figs. 4(a) and 4(b). According to the evolution of $|\beta_2|$, the nuclear shape seems approaching to the spherical shape with increasing the neutron number.

B. Magnetic dipole moment of odd-even iridium isotope ^{197}Ir

We calculated the magnetic dipole moment of iridium isotopes by using its expressions in the strong coupling scheme [45]:

$$\mu = g_R I + (g_K - g_R)\frac{K^2}{I+1}\quad (K > 1/2), \tag{15}$$

$$\mu = g_R I + \frac{g_K - g_R}{4(I+1)}\left(1 + (2I+1)(-1)^{I+1/2}b\right)(K = 1/2), \tag{16}$$

where g_R and g_K are the g factors associated with the collective motion of the core and the particle motion in the deformed nucleus, respectively. K is the projection of the nuclear spin on the deformation symmetry axis and is equal to I for the nuclear ground state. b is a magnetic decoupling parameter given in Eq. (4 A-12) in Ref. [45]. g_R is usually given by the ratio of atomic number and mass number of the core nucleus: $g_R = Z_{\rm core}/A_{\rm core}$. According to Fig. (4-6) in Ref. [45], the observed g_R values are mostly smaller than $Z_{\rm core}/A_{\rm core} \approx 0.39$ and larger than 0.2 in this nuclear region. Therefore, we calculated the μ values in the cases of $g_R = Z_{\rm core}/A_{\rm core}$ and 0.2.

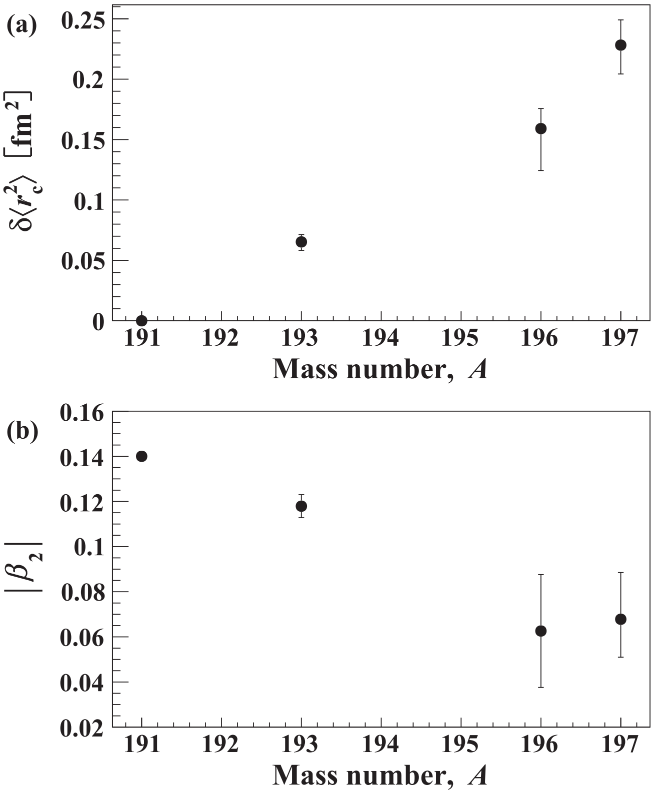

FIG. 4. (a) Variation of mean-square charge radii and (b) absolute values of quadrupole deformation parameters for the iridium isotopes with mass numbers $A \geqslant 191$. The black dots refer to the values in this work. The $|\beta_2|$ values were normalized to be $\beta_2 = +0.140$ at ^{191}Ir, which was calculated from the Q value.

TABLE V. The experimental μ_{exp} and theoretical μ_{cal} values of odd-A Ir isotopes with $N = 112$–120 and $I^{\pi} = 3/2^{+}$. The μ_{cal} values were obtained by using the tabulated β_2 values. $\beta_2 = +0.151(2), +0.140(2), +0.128(2)$ of ^{189,191,193}Ir were deduced from the previously measured Q values of them.

	N	Q (b)	β_2	μ_{exp} (μ_{N})	μ_{cal} (μ_{N})	
					$g_R = Z_{\mathrm{core}}/A_{\mathrm{core}}$	$g_R = 0.2$
^{189}Ir	112	+0.878(10) [47]	+0.151(2)	+0.147(7) [3]	$+0.146^{+0.003}_{-0.005}$	$+0.145^{+0.003}_{-0.004}$
^{191}Ir	114	+0.816(9) [32]	+0.140(2)	+0.1507(6) [24]	–	–
^{193}Ir	116	+0.751(9) [32]	+0.128(2)	+0.1636(6) [24]	$+0.159^{+0.003}_{-0.005}$	$+0.160^{+0.003}_{-0.005}$
			+0.118(5)[a]		$+0.169^{+0.007}_{-0.008}$	$+0.169^{+0.006}_{-0.008}$
^{197}Ir	120	–	+0.07(2)[a]	$+0.27^{+0.10}_{-0.03}$[a]	$+0.23^{+0.04}_{-0.04}$	$+0.23^{+0.04}_{-0.03}$
			−0.07(2)[a]		$+1.0^{+0.2}_{-0.2}$	$+0.9^{+0.2}_{-0.2}$

[a] This work.

g_K is calculated from the expression (Eq. (5-86) in Ref. [45])

$$g_K = \frac{1}{\Omega}(g_l\Omega + (g_s - g_l)\langle\Omega|\hat{s}_3|\Omega\rangle) \quad (\Omega \neq 1/2), \tag{17}$$

where Ω is the projected angular momentum of the valence nucleon, g_s and g_l are the spin and orbital g factors associated with the motion of valence nucleon, and $\hat{s}_3$ is the nucleon spin operator along the deformation symmetry axis. The g_l value is 1 for the proton or 0 for the neutron.

b in Eq. (16) and the expectation value of $\hat{s}_3$ in Eq. (17) were obtained from a theoretical calculation which describes eigenstates of the nucleus as a one-particle plus core in the axially symmetric quadrupole-deformed potential [46]. The details of the calculation are given in Ref. [46] and references therein. In the theoretical calculation, the values describing the one-body potential were determined similarly as mentioned in Ref. [46].

g_s is generally expressed as $g_s = f g_s^{\mathrm{free}}$, where g_s^{free} is bare spin g factor and takes +5.586 for the proton and −3.826 for the neutron, and the f is a coefficient taking care of core-polarization. Here, the f values of $0.854^{+0.002}_{-0.001}$ and $0.772^{+0.002}_{-0.001}$ were determined by assuming $g_R = Z_{\mathrm{core}}/A_{\mathrm{core}}$ and 0.2, respectively, to reproduce the experimental μ_{exp} value of ^{191}Ir in the calculations. The uncertainty of f is originated from the uncertainties of μ_{exp} and β_2 of ^{191}Ir. The β_2 value was required in the theoretical calculation to describe the axially symmetric quadrupole-deformed potential.

Table V shows the μ_{exp} and μ_{cal} values of odd-A Ir isotopes with $N = 112$–120 and $I^{\pi} = 3/2^{+}$. In the calculations, we used the β_2 values of +0.151(2) and +0.128(4) for ^{189}Ir and ^{193}Ir, respectively. These values were estimated from the previously measured spectroscopic Q values: $Q = +0.878(10)$ b of ^{189}Ir [47] and $Q = +0.751(9)$ b of ^{193}Ir [32] assuming $K = I = 3/2$. As shown in the table, the g_R value does not affect the results of μ_{cal}. The uncertainty of μ_{cal} values originate from the uncertainty of β_2 of each isotope and from the uncertainty of f. The μ_{exp} values of all the isotopes were reproduced by the μ_{cal} values. From the agreement between the μ_{exp} and μ_{cal} values, it is quite reasonable to assign positive sign to the β_2 (prolate deformation) of ^{197}Ir. Even though small β_2 of ^{197}Ir, this nucleus can be interpreted as being prolately deformed, as light iridium isotopes are [3].

C. Magnetic dipole moment of odd-odd iridium isotopes ^{196,198}Ir

We estimated the μ values of ^{196,198}Ir from a combination of experimental g_K values of neighboring nuclei based on the strong coupling model. The g_K values of ^{196,198}Ir were calculated from the expressions [48] as

$$g_K = g_\Omega \equiv \frac{1}{\Omega}(\Omega_{\mathrm{p}} g_{\Omega_{\mathrm{p}}} + \Omega_{\mathrm{n}} g_{\Omega_{\mathrm{n}}}), \tag{18}$$

$$\Omega = \Omega_{\mathrm{p}} + \Omega_{\mathrm{n}}, \tag{19}$$

where Ω_i and g_{Ω_i} are the projected angular momentum and g-factor of the valence nucleon (i = p, n), respectively. g_{Ω_i} was calculated by substituting an experimental μ_{exp} value of the neighboring nucleus into Eq. (15) or (16).

To calculate the g_{Ω_i} values, we chose the nuclei which have the same proton or neutron numbers as ^{196,198}Ir ($Z = 77$, $N = 119, 121$). Those are ^{197}Ir ($Z = 77$, $N = 120$) for proton $g_{\Omega_{\mathrm{p}}}$ and ^{197,199}Pt ($Z = 78$, $N = 119, 121$) for neutron $g_{\Omega_{\mathrm{n}}}$. Here, we used the μ_{exp} values of ^{197,199}Pt instead of ^{195,197}Os ($Z = 76$, $N = 119, 121$) because their μ_{exp} values have not been measured. The $g_{\Omega_{\mathrm{p}}}$ value was calculated from $\mu = +0.27^{+0.10}_{-0.03}\ \mu_{\mathrm{N}}$ of ^{197}Ir, evaluated in this work. The μ and I^{π} values of ^{197}Pt and ^{199}Pt are reported to be $\mu = (+)0.51(2)\ \mu_{\mathrm{N}}$ [49], $I^{\pi} = 1/2^{-}$ and $\mu = +0.75(8)\ \mu_{\mathrm{N}}$ [26], $I^{\pi} = 5/2^{-}$, respectively. The positive sign of μ of ^{197}Pt was assumed based on the HFB calculations introduced in Ref. [26]. In the case of ^{197}Pt with $K = 1/2$, the $g_{\Omega_{\mathrm{n}}}$ value was calculated by using Eq. (16) with the b value obtained from the theoretical calculation, as mentioned in the previous section, Sec. V B, by assuming $\beta_2 = -0.131$ predicted by the HFB calculation [26] in the cases of $g_R = Z_{\mathrm{core}}/A_{\mathrm{core}}$ and 0.2.

From the comparison between the μ_{cal} and μ_{exp} values, the most probable coupling combinations were listed in Table VI. As shown in the table, the g_R value does not affect the results of μ_{cal} except in the case $K = 0,\ I = 1$. The uncertainty of μ_{cal} values are originated from the uncertainties of μ_{exp} values of the neighboring nuclei. The pairs of μ_{exp} and I^{π} values of ^{196}Ir can be explained in all the coupling combinations of Ω_{p} and Ω_{n} with $I^{\pi} = 1^{-}$ or 2^{-}. The μ_{exp} value of ^{198}Ir can be explained by coupling combinations with $I^{\pi} = 1$. As a result, we can suggest $I^{\pi} = 1, 2^{-}$ for ^{196}Ir and $I^{\pi} = 1^{-}$ for ^{198}Ir. In order to discuss the nuclear structure based on the estimated wave functions, we need to determine more precisely μ_{exp}

TABLE VI. The calculated μ_{cal} values of ^{196,198}Ir based on the strong coupling model.

	Ω_p	Ω_n	K	I	μ_{cal} (μ_N)		μ_{exp} (μ_N)
					$g_R = Z_{\text{core}}/A_{\text{core}}$	$g_R = 0.2$	
^{196}Ir	1.5	0.5	2	2	$+0.39^{+0.11}_{-0.04}$	$+0.40^{+0.11}_{-0.04}$	$+0.34^{+0.05}_{-0.14}$
	1.5	−0.5	1	1	$+0.15^{+0.09}_{-0.03}$	$+0.15^{+0.09}_{-0.03}$	$+0.31^{+0.04}_{-0.20}$
	0.5	0.5	1	1	$+0.28^{+0.03}_{-0.01}$	$+0.21^{+0.03}_{-0.01}$	
	–	–	0	1	+0.39	+0.20	
^{198}Ir	1.5	−0.5	1	1	$+0.16^{+0.09}_{-0.04}$	$+0.14^{+0.09}_{-0.04}$	$+0.13^{+0.10}_{-0.02}$
	0.5	0.5	1	1	$+0.27^{+0.04}_{-0.02}$	$+0.23^{+0.04}_{-0.02}$	
	–	–	0	1	+0.39	+0.20	

values of ^{196,198}Ir and neighboring nuclei from measured HFS spectra with improved resolution by applying in-gas-jet laser ionization spectroscopy [50] at KISS.

VI. SUMMARY

The HFS measurements of ^{196,197,198}Ir were performed via in-gas-cell laser resonance ionization spectroscopy at KISS to determine nuclear magnetic dipole moments and isotope shifts. The magnetic dipole moment μ of ^{197}Ir ($I^\pi = 3/2^+$) was determined to be $+0.27^{+0.10}_{-0.03}$ μ_N. For ^{196}Ir [$I^\pi = (0^-)$] and ^{198}Ir ($I^\pi =$ unknown), the reduced χ^2 fitting analyses strongly indicated the spin value of $I > 0$. Possible combinations of I^π and μ_{exp} are suggested from the fitting analyses.

The variation of nuclear mean-square charge radius $\delta\langle r_c^2\rangle^{191,A'}$ and quadrupole deformation parameter $|\beta_2|$ were extracted from the measured isotope shift taking into account the nuclear charge distribution by considering the axial symmetric quadrupole deformation and higher order of electronic factors computed using the atomic structure RIS4 code. We deduced $\delta\langle r_c^2\rangle^{191,A'} = +0.16^{+0.03}_{-0.02}$ fm^2, $|\beta_2| = 0.06(2)$ for ^{196}Ir and $\delta\langle r_c^2\rangle^{191,A'} = +0.23(2)$ fm^2, $|\beta_2| = 0.07(2)$ for ^{197}Ir.

The μ value of ^{197}Ir agreed with a theoretical value based on the strong coupling model, and the Ir nucleus was interpreted as prolately deformed by the theoretical calculations.

The μ values of ^{196,198}Ir were calculated semiempirically based on the strong coupling model, and these values were compared with the experimental values. From the comparison, we can suggest the possible spin values of $I^\pi = 1, 2^-$ for ^{196}Ir and $I^\pi = 1^-$ for ^{198}Ir with some coupling combinations of Ω_p and Ω_n.

To determine the spin value and discuss nuclear structure from the estimated wave function, it is necessary to perform the laser spectroscopy with the resolution of less than 1 GHz by using in-gas-jet laser ionization technique. The developments in that direction are ongoing at KISS.

ACKNOWLEDGMENTS

The experiments were performed at the RI Beam Factory (RIBF) operated by RIKEN Nishina Center and CNS, University of Tokyo. The experiments were performed under Program No. NP1512-RRC41 at the RIBF. We gratefully acknowledge Prof. I. Hamamoto (RIKEN, Japan) for the communications and discussions of the relevant physics for the calculations of magnetic moments in the strong coupling model by using her computer program. M.M. acknowledges the support from RIKEN as a Junior Research Associate (JRA). This work was supported by JSPS KAKENHI Grants No. JP24740180, No. JP26247044, No. JP15H02096, and No. JP17H01132. M.G. and S.S. acknowledge support from the FWO & FNRS Excellence of Science Programme (EOS-O022818F) for the atomic physics calculations. S.S. is a FRIA grantee of the F.R.S-FNRS.

[1] M. Mumpower, J. Cass, G. Passucci, R. Surman, and A. Aprahamian, AIP Adv. **4**, 041009 (2014).

[2] K. Langanke and G. Martínez-Pinedo, Rev. Mod. Phys. **75**, 819 (2003).

[3] D. Verney *et al.*, Eur. Phys. J. A **30**, 489 (2006).

[4] G. Ulm *et al.*, Z. Phys. A **325**, 247 (1986).

[5] K. Wallmeroth *et al.*, Nucl. Phys. A **493**, 224 (1989).

[6] Th. Hilberath, St. Beckcr, G. Bollen, H.-J. Kluge, U. Krönert, G. Passler, J. Rikovska, R. Wyss, and the ISOLDE Collaboration, Z. Phys. A **342**, 1 (1992).

[7] P. Möller, J. R. Nix, W. D. Myers, and W. J. Swiatecki, At. Data Nucl. Data Tables **59**, 185 (1995).

[8] Y. Hirayama *et al.*, Nucl. Instrum. Methods Phys. Res. B **353**, 4 (2015).

[9] Y. Hirayama *et al.*, Nucl. Instrum. Methods Phys. Res. B **376**, 52 (2016).

[10] Y. Hirayama *et al.*, Nucl. Instrum. Methods Phys. Res. B **412**, 11 (2017).

[11] H. Xiaolong, Nucl. Data Sheets **108**, 1093 (2007).

[12] H. Xiaolong and Z. Chunmei, Nucl. Data Sheets **104**, 283 (2005).

[13] H. Xiaolong, Nucl. Data Sheets **110**, 2533 (2009).

[14] J. F. W. Jansen, H. Pauw, and C. J. Toeset, Nucl. Phys. A **115**, 321 (1968).

[15] J. A. Cizewski, D. G. Burke, E. R. Flynn, R. E. Brown, and J. W. Sunier, Phys. Rev. C **27**, 1040 (1983).

[16] G. T. Emery, in *Springer Handbook of Atomic, Molecular, and Optical Physics*, edited by G. W. F. Drake (Springer-Verlag, New York, 2006), p. 253.

[17] C. Wraith *et al.*, Phys. Lett. B **771**, 385 (2017).

[18] D. T. Yordanov *et al.*, Commun. Phys. **3**, 107 (2020).

[19] Y. X. Watanabe *et al.*, Phys. Rev. Lett. **115**, 172503 (2015).

[20] S. Kimura *et al.*, Nucl. Instrum. Methods Phys. Res. B **376**, 338 (2016).

[21] M. Mukai *et al.*, Nucl. Instrum. Methods Phys. Res. A **884**, 1 (2018).

[22] Th. A. M. Van Kleef, Physica **23**, 843 (1957).

[23] "NIST Atomic Spectra Database Lines Data," https://physics.nist.gov/PhysRefData/ASD/lines_form.html.

[24] K. H. Bürger, S. Büttgenbach, R. Dicke, G. Gölz, and F. Träber, Phys. Lett. B **140**, 17 (1984).

[25] R. P. de Groote, M. Verlinde, V. Sonnenschein, K. T. Flanagan, I. Moore, and G. Neyens, Phys. Rev. A **95**, 032502 (2017).

[26] Y. Hirayama *et al.*, Phys. Rev. C **96**, 014307 (2017).

[27] T. Sonoda, T. E. Cocolios, J. Gentens, M. Huyse, O. Ivanov, Yu. Kudryavtsev, D. Pauwels, P. Van den Bergh, and P. Van Duppen, Nucl. Instrum. Methods Phys. Res. B **267**, 2918 (2009).

[28] I. V. Hertel and C.-P. Schulz, *Atoms, Molecules and Optical Physics 1: Atoms and Spectroscopy* (Springer-Verlag, Berlin/Heidelberg, 2015), p. 227.

[29] U. Köster *et al.*, Phys. Rev. C **84**, 034320 (2011).

[30] "ROOT, a data analysis framework," https://root.cern.ch.

[31] F. James, "MINUIT: Function minimization and error analysis, CERN program library entry d506," https://root.cern.ch/download/minuit.pdf.

[32] Y. Tanaka, R. M. Steffen, E. B. Shera, W. Reuter, M. V. Hoehn, and J. D. Zumbro, Phys. Rev. C **29**, 1830 (1984).

[33] S. A. Ahmad, W. Klempt, R. Neugart, E. W. Otten, P.-G. Reinhard, G. Ulm, and K. Wendt, Nucl. Phys. A **483**, 244 (1988).

[34] J. Ekman, P. Jönsson, M. Godefroid, C. Nazé, G. Gaigalas, and J. Bieroń, Comput. Phys. Commun. **235**, 433 (2019).

[35] S. Schiffmann and M. Godefroid, J. Quant. Spectrosc. Radiat. Transfer 107332 (2020).

[36] C. Froese Fischer, G. Gaigalas, P. Jönsson, and J. Bieroń, Comput. Phys. Commun. **237**, 184 (2019).

[37] C. Froese Fischer, M. Godefroid, T. Brage, P. Jönsson, and G. Gaigalas, J. Phys. B **49**, 182004 (2016).

[38] C. E. Moore, *Atomic Energy Levels as Derived From the Analyses of Optical Spectra*, Vol. III (National Bureau of Standards, Washington, DC, 1971), p. 178.

[39] E. Belin *et al.*, *Pt Platinum: Platinum-Group Metals: Isotopes, Atoms, Molecules, Clusters* (Springer Science & Business Media, New York, 2013).

[40] I. P. Grant, *Relativistic Quantum Theory of Atoms and Molecules. Theory and Computation* (Springer, New York, 2007).

[41] H. L. Xu, S. Svanberg, P. Quinet, P. Palmeri, and E. Biémont, J. Quant. Spectrosc. Radiat. Transfer **104**, 52 (2007).

[42] J. Bauche and R.-J. Champeau, Adv. At. Mol. Phys. **12**, 39 (1976).

[43] Y. Ishida, H. Iimura, S. Ichikawa, and T. Horiguchi, J. Phys. B **30**, 2569 (1997).

[44] D. Berdichevsky and F. Tondeur, Z. Phys. A **322**, 141 (1985).

[45] A. Bohr and B. R. Mottelson, *Nuclear Structure Volume II: Nuclear Deformations* (World Scientific Publishing Co. Pte. Ltd., Singapore, 1998).

[46] I. Hamamoto, Phys. Rev. C **99**, 024319 (2019).

[47] G. Seewald, E. Hagn, B. Hinfurtner, E. Zech, D. Forkel-Wirth, R. Eder, and the ISOLDE Collaboration, Phys. Rev. Lett. **77**, 5016 (1996).

[48] A. Bohr and B. R. Mottelson, Mat. Fys. Medd. K. Dan. Vidensk. Selsk. **27**, 16 (1953).

[49] T. Ohtsubo, S. Ohya, Y. Masamori, T. Izumikawa, S. Muto, and K. Nishimura, Hyperfine Interact. **198**, 143 (2010).

[50] Yu. Kudryavtsev, R. Ferrer, M. Huyse, P. Van den Bergh, and P. Van Duppen, Nucl. Instrum. Methods Phys. Res. B **297**, 7 (2013).